Supporting Information

Mechanistic Mapping of Alkali-Ion Storage in Micro-Spherical Closed-Pores Hard Carbon: Electrochemical, *Ex-Situ*, and DFT Approaches

Authors: Nagmani [1,2,3*], Deepak Kumar Gorai [2], Priyanka Pal,[3] Sanchita Manna,[1] Raju Kumar Gupta [2,3] and Sreeraj Puravankara [1*]

Affiliations: [1] School of Energy Science & Engineering, Indian Institute of Technology Kharagpur, Kharagpur -721302, West Bengal, India

[2] Department of Sustainable Energy Engineering, Indian Institute of Technology Kanpur, Kanpur-208016, Uttar Pradesh, India

[3]Department of Chemical Engineering, Indian Institute of Technology Kanpur, Kanpur-208016, Uttar Pradesh, India

Corresponding author: Dr. Nagmani
Department of Sustainable Energy Engineering
Indian Institute of Technology Kanpur
Kanpur-208016, Uttar Pradesh, India
Phone- +91-9709584593
Email: nagmani@iitkgp.ac.in

Dr. Sreeraj Puravankara
School of Energy Science & Engineering,
Indian Institute of Technology Kharagpur
Kharagpur -721302, West Bengal, India
Phone (Office) - +913222 260801
email: sreeraj@iitkgp.ac.in

ORCID ID

Nagmani: https://orcid.org/0000-0003-4618-4952

Sreeraj Puravankara: https://orcid.org/0000-0002-9238-0148

Experimental Section:

Synthesis and Characterization: Figure 1 shows a schematic illustration of the hard carbon synthesis process based on microwave-assisted solvothermal pre-treatment followed by the single-step carbonization methods from our recent study.[1] To investigate the nanostructure of the sample, high-resolution transmission electron microscopy (HR-TEM, JEOL, JEM-2100) was performed. The intrinsic defects of the sample were characterized using X-ray diffraction (XRD, Bruker-D2 Phaser) instrument with Cu Kα (λ = 1.5418 Å) radiation. The sample's morphology was observed by field-emission gun-scanning electron microscopy (FEG-SEM, ZEISS Sigma 300). Further, the defect structures were analysed by Raman spectroscopy using Horiba T6400 with a 514.5 nm Ar-Krypton mixed ion gas laser. Besides, the surface chemistry and extrinsic defects of the sample were investigated using X-ray photoelectron spectroscopy (XPS) using a monochromatic Al K_α X-Ray Source on PHI 5000 VERSA PROBE III (ULVAC PHI (Physical Electronics), USA) XPS instrument. The porosity information, such as surface area and pore size distribution, was characterized using the nitrogen adsorption/desorption isotherm on the Autosorb IQ instrument at 77K with an outgassing temperature of 200 °C. In addition, to insight into the closed porosity of the sample, SAXS was employed, using a XENOCS SAS instrument using synchrotron radiation as the X-ray source (30 W Cu tube with 50KV, 0.6 mA). Moreover, the ex-situ Raman and XPS characterization was performed on the cycled hard carbon electrode on the same instrument. The cycled electrodes' ex-situ electron paramagnetic resonance (EPR) measurements were performed on Bruker ELEXSYS 580 EPR spectrometer as a first derivative of the absorption signal in the X-band (9.6 GHz) at room temperature. The microwave power and modulation amplitude were used as 15 mW and 5 G, respectively. In addition, operando XRD during cell operation were collected using the same XRD instrument (Bruker-D2 Phaser) with Cu Kα radiation.

Preparation of Hard Carbon Anode: A homogeneous slurry was prepared by mixing hard carbon, Super-P black carbon, and polyvinylidene difluoride (PVDF, Sigma-Aldrich) in the mass ratio of 8:1:1, using the mortar and pestle for 1 hr, followed by addition of N-methyl-2-pyrrolidone solvent (NMP, Sigma-Aldrich, 99.5%). The hard carbon electrode was prepared by coating the slurry onto the Cu foil and dried at 80℃ in a vacuum oven for 12 h. After that, the electrode was cut into 15 mm diameter with a mass loading of ~ 2 mg cm^{-2}.

Electrochemical Characterization: The stainless-steel coin cells (CR-2032) were fabricated inside the Ar-filled glovebox (M-Braun, H_2O < 0.5 ppm; O_2 < 0.5 ppm). In half-cell configuration, Li/Na/K metal (10 mm in diameter) and Glass fibre membrane (GF/C, 19 mm in diameter) from Whatman were used as the counter electrode and as the separator, respectively. We prepared 1M $LiPF_6$/$NaPF_6$/KPF_6 (Sigma-Aldrich, 98%) salt-based electrolyte in a binary solvent of ethylene carbonate (EC) and diethyl carbonate (DEC) (1:1 % v/v, Sigma Aldrich)). All galvanostatic charge-discharge (GCD) profiles and cycling performance at different current rates and cyclic voltammetry (CV) at different scan rates were tested using the Bio-Logic battery testing instrument in the potential range of 1.5 to 0.005 V. The galvanostatic intermittent titration technique (GITT) was employed at a 0.1 C rate for 30 min and then relaxed for two hours until the potential reached 5 mV. Electrochemical impedance spectroscopy (EIS) was conducted from a high frequency of 100 kHz to a low frequency of 10 kHz.

Computational Methods: The projected augmented wave (PAW) approach as implemented in the Vienna Ab initio Simulation Package (VASP) was used for all the spin-polarized density functional theory (DFT) calculations.[2,3] The Perdew-Burke-Ernzerhof (PBE) exchange-correlation functional in the generalized gradient approximation (GGA) scheme was used to explain the electron interactions.[4] The kinetic cutoff energy of 500 eV was used for the plane-

wave basis set. The DFT-D3 approach of Grimme with zero damping was used for van der Waals forces between graphitic sheets.[5]

In order to build the planar graphitic layers model, an AB stacking mode of two graphitic layers was used. The interlayer distance was altered to determine how it affected the binding energy of the alkali-ion. The top and lower surfaces were always separated by a vacuum layer thickness of 18 Å along the z-direction. At each interlayer distance, the inserted metal ion was totally released, and the two graphitic layers were fixed to maintain the interlayer spacing. In contrast, single-walled carbon nanotubes of varying diameters were used to simulate the micropores. After being completely relaxed, the alkali-ion was introduced into the carbon layers. In all computations, the structural optimization was considered finished when the forces on the atoms were less than 0.02 eV $Å^{-1}$. The binding energy ($\triangle E_b$) of an alkali ion in carbon models was determined as follows:

$$\triangle E_b = E_{X\text{-}carbon} - \mu_X - E_{carbon}$$

where $E_{X\text{-}carbon}$ is the total energy of the carbon models with an added alkali-ion, μ_{ion} is the chemical potential of the alkali-ion, which was determined from the alkali crystal, and E_{carbon} is the energy of the carbon system.

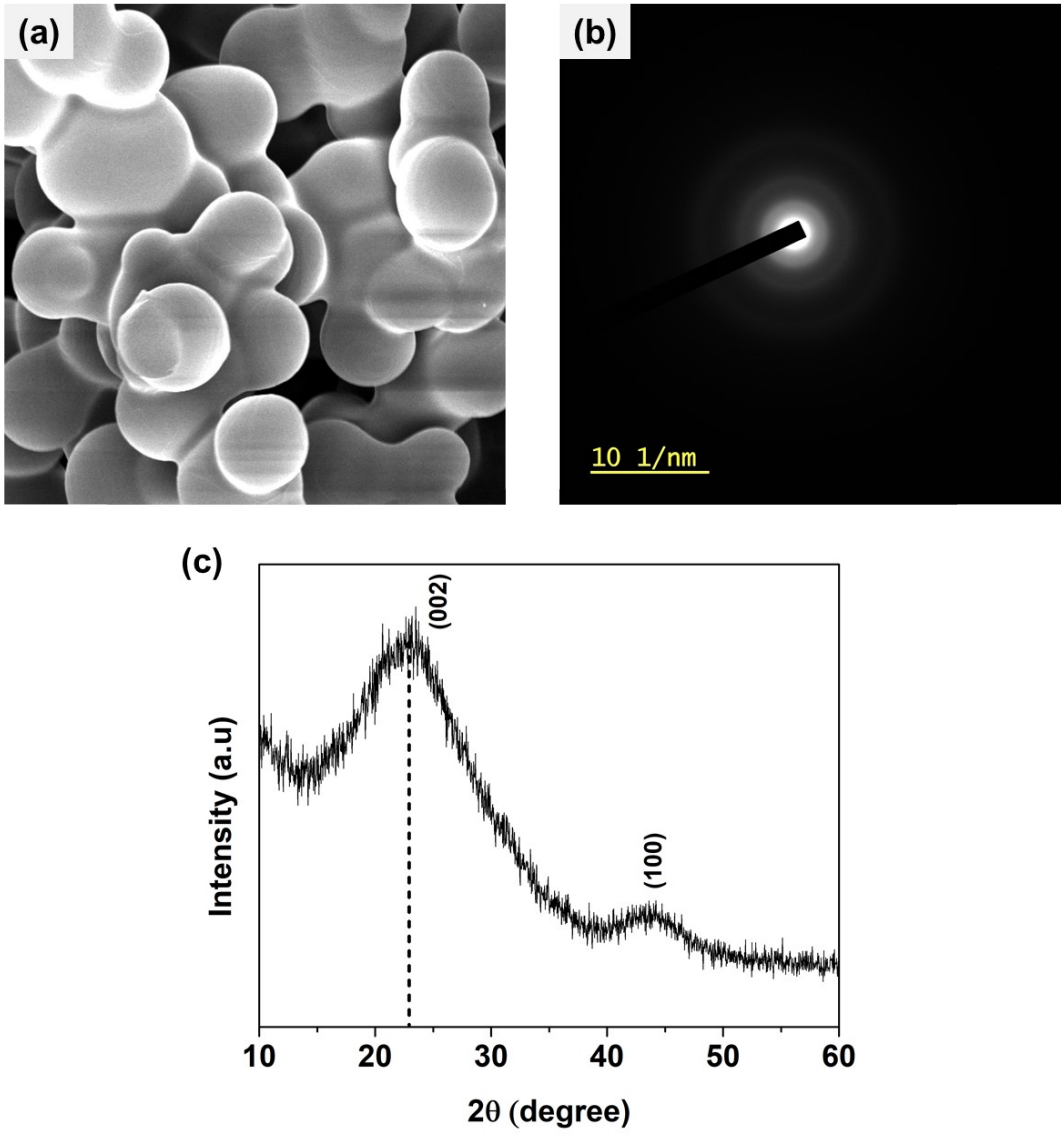

Figure S1: (a) SEM Image of MSHC before heat-treatment carbonization, (b) SAED pattern, and (c) XRD pattern of MSHC.

SAXS Data Processing and analysis: The primary data processing such as scattering vector (or scattering angle) calibration, normalization of the incident beam intensity and background substraction is performed by knowing the incident X-ray wavelength (λ = 1.54 Å) and sample to detector disctance.[6]

Guinier Analysis: The Guinier formula holds at small q region to evaluate the size of the particles.[6–8] It is expressed as the following:

$$\ln I(q) = \ln I(0) - (qR_G)^2/3 \quad \text{(S1)}$$

$$R_G = \sqrt{\frac{3}{5}} \times \frac{D}{2} \quad \text{(S2)}$$

where, I (0) is the scattering intensity at q = 0, R_G is the radius of gyration, and D is the diameter of the pore (assumed as spherical in morphology). Figure shows the Guinier plots for MSHC

Porod Analysis: Porod's law is one of the basic methods in SAXS to quantify the porod constant for the calculation of the specific surface area of the sample. Porod's law suggests that the $q^4I(q)$ value will approach a constant K (Porod constant) when q increases to a certain level without any deviation and it can be expressed as equation (S3):[6–8]

$$\lim q^4 I(q) = K \quad \text{or} \quad \lim \ln[q^4 I(q)] = \ln K \quad \text{(S3)}$$

where q is the scattering vector, $q = 4\pi \sin\theta/\lambda$, 2θ is the scattering angle, λ is the incident X-ray wavelength, I(q) is the scattering intensity, K is the porod constant.

Herein, the positive deviation will arise in the porod plot, suggesting some additional scattering. A correction factor like exp (bq^2) might be used to rectify the positive deviation, and the Porod constant (K) can be expressed as equation (S4).[6,7]

$$\ln [q^4 I(q)] = \ln K + bq^2 \quad \text{(S4)}$$

The specific surface area (S) of the samples can be calculated by the following equation (S5):

$$S = \pi P\,(1-P)K/Q \qquad \text{(S5)}$$

Where, P is the volume fraction for porous system called as porosity; Q is the invariant which is given by $Q = \int_0^{\infty} q^2 I(q)dq$ (S6)

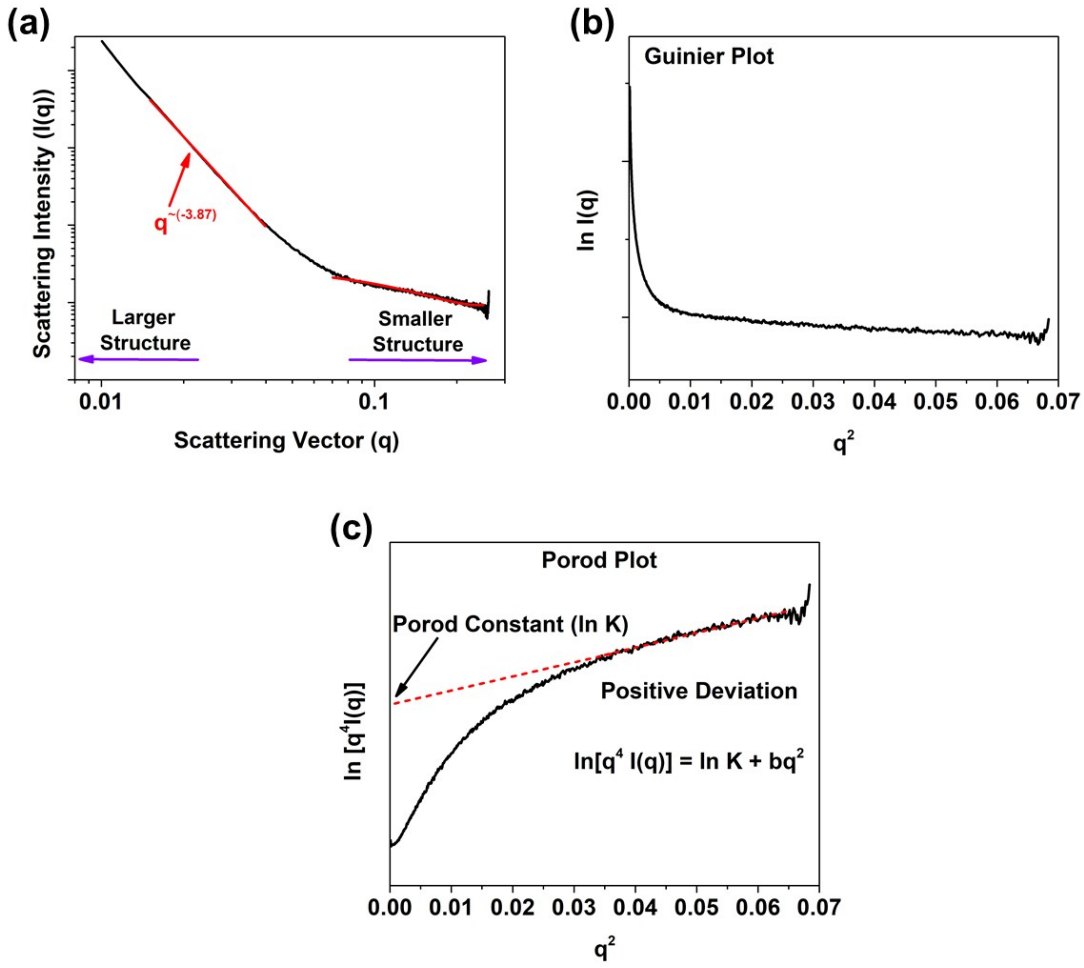

Figure S2: (a) SAXS pattern, (b) Guinier plots, and (c) porod plot of MSHC.

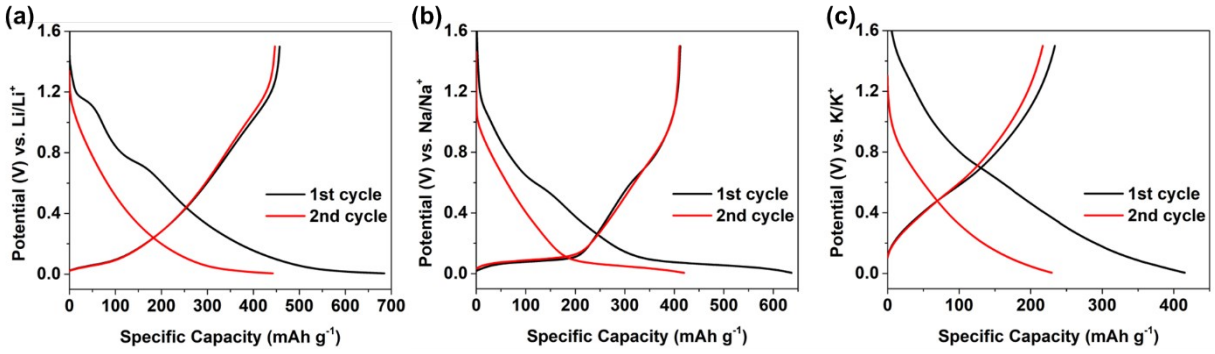

Figure S3: Galvanostatic charge-discharge profile at the current rate of 0.1 C for (a) MSHC/Li, (b) MSHC/Na and (c) MSHC/K.

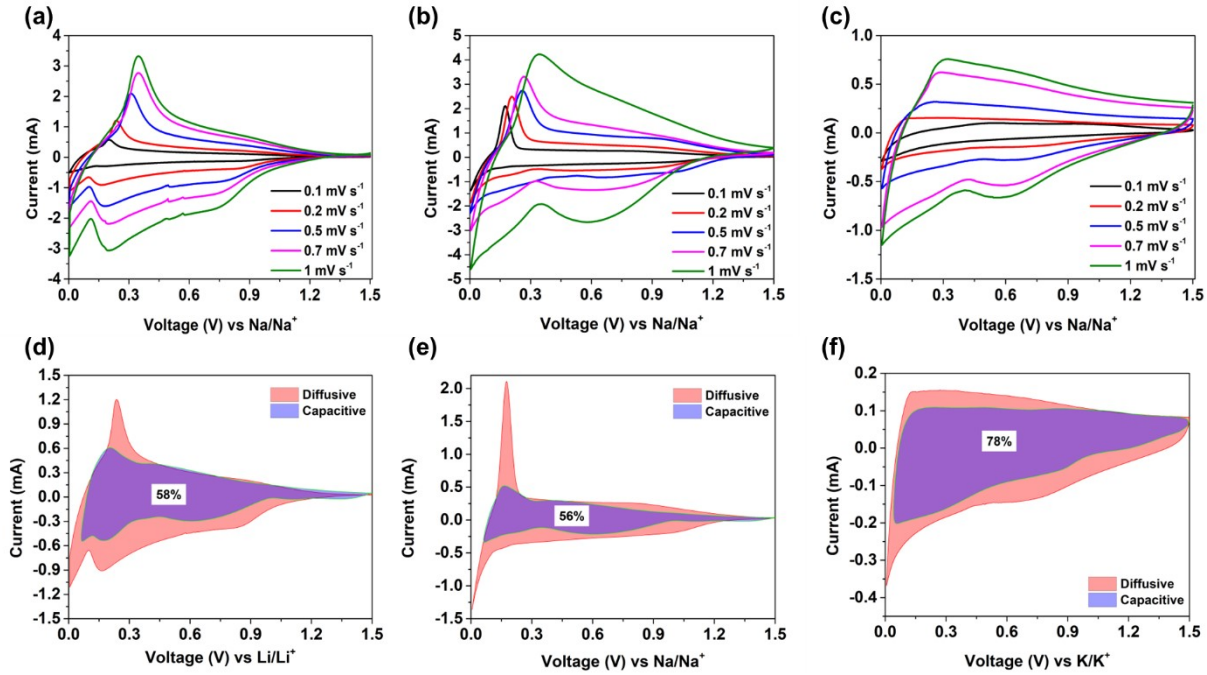

Figure S4: (a) Combined CV curve at the scan rate of 0.1 mV s^{-1}. Relationship between logarithm current peak and logarithm scan rate for (b) MSHC/Li, (c) MSHC/Na, and (d) MSHC/K.

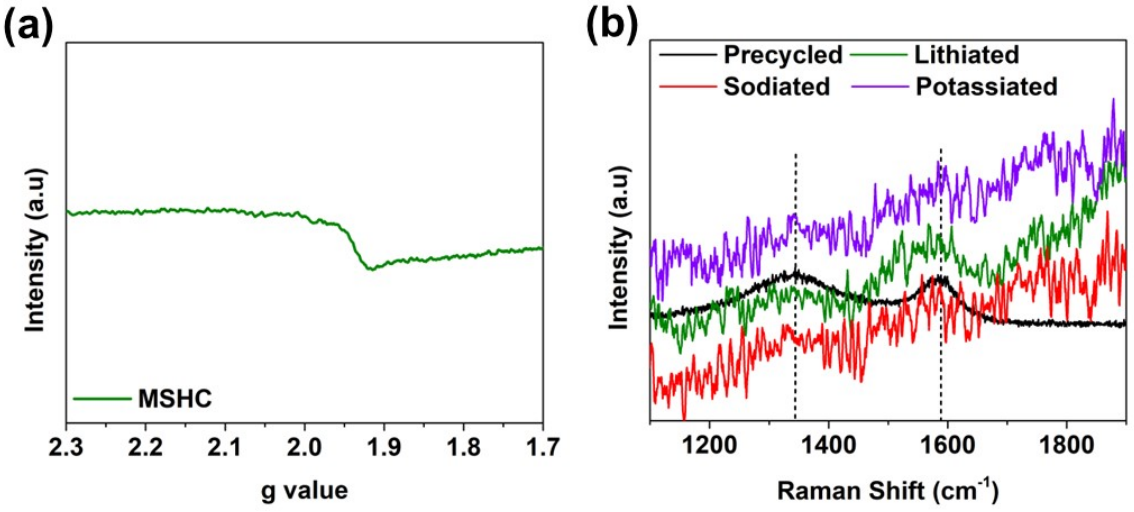

Figure S5: (a) EPR of hard carbon (MSHC) and (b) ex-situ Raman spectra of discharge MSHC electrode to 5 mV.

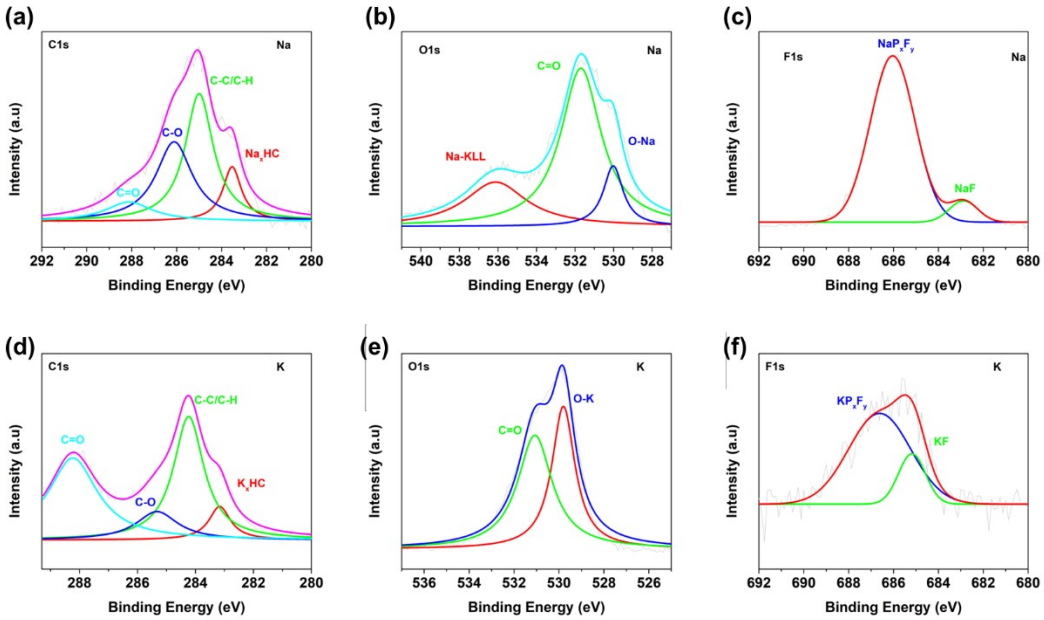

Figure S6: XPS deconvoluted (a,d) C-1s, (b,e) O-1s and (c,f) F-1s spectra of cycled MSHC electrode in Na-system and K-system.

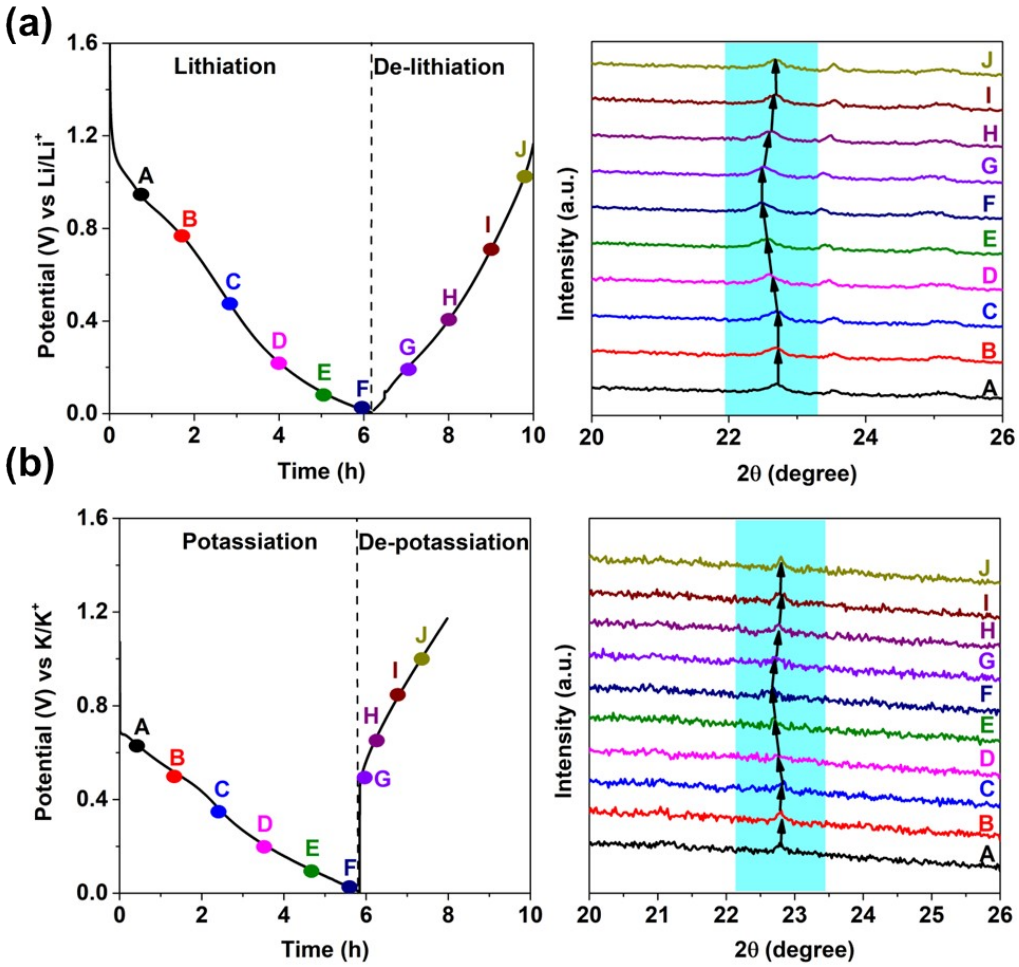

Figure S7: Operando XRD patterns of the MSHC electrode in (a) Li-, and (b) K-ion cells recorded during the first discharge–charge cycle at a current density of 50 mA g^{-1} at room temperature.

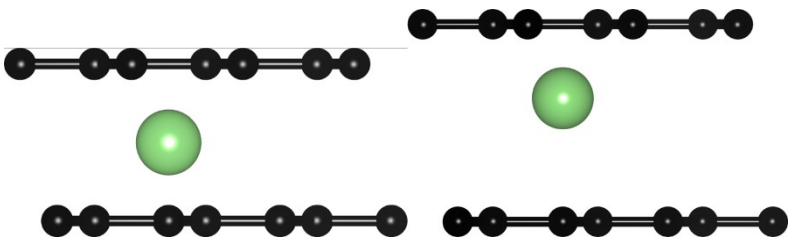

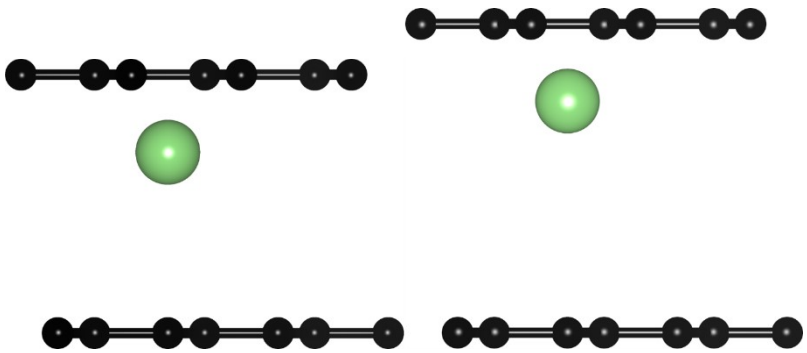

Figure S8: Configurations of Li ion inserted into the planar graphitic layer with (a) 3 Å, (b) 4 Å, (c) 5 Å, and (d) 6 Å interlayer distances.

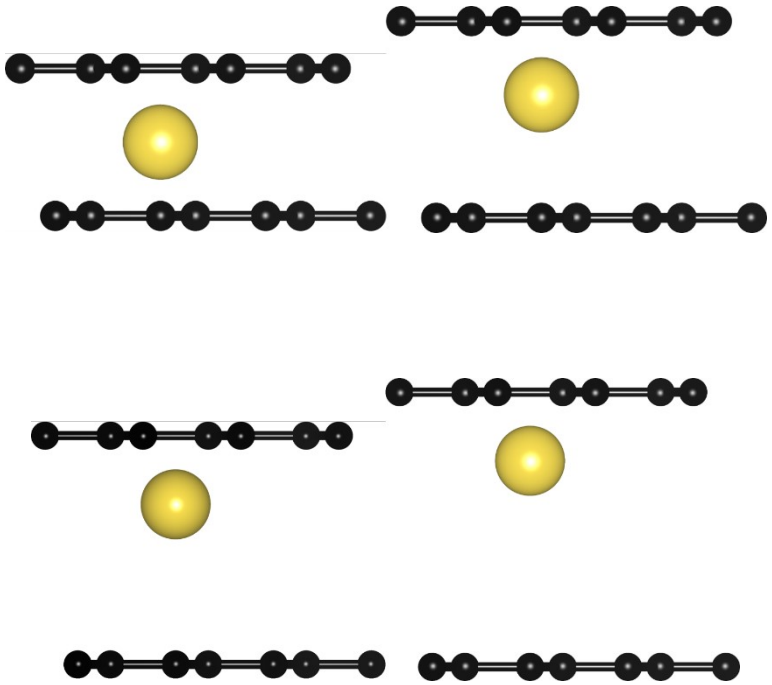

Figure S9: Configurations of Na ion inserted into the planar graphitic layer with (a) 3 Å, (b) 4 Å, (c) 5 Å, and (d) 6 Å interlayer distances.

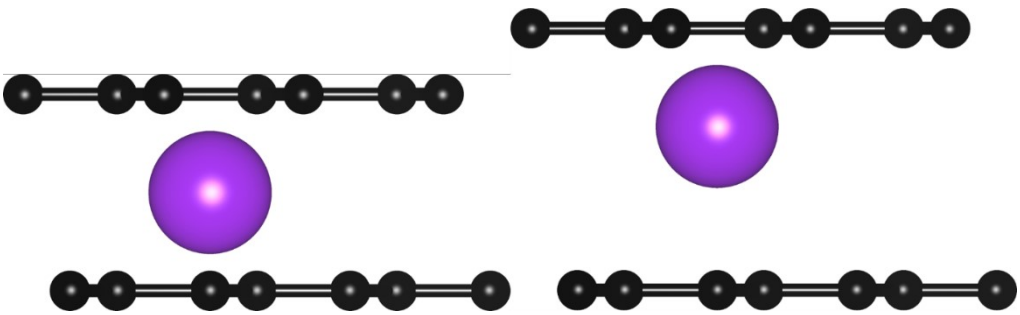

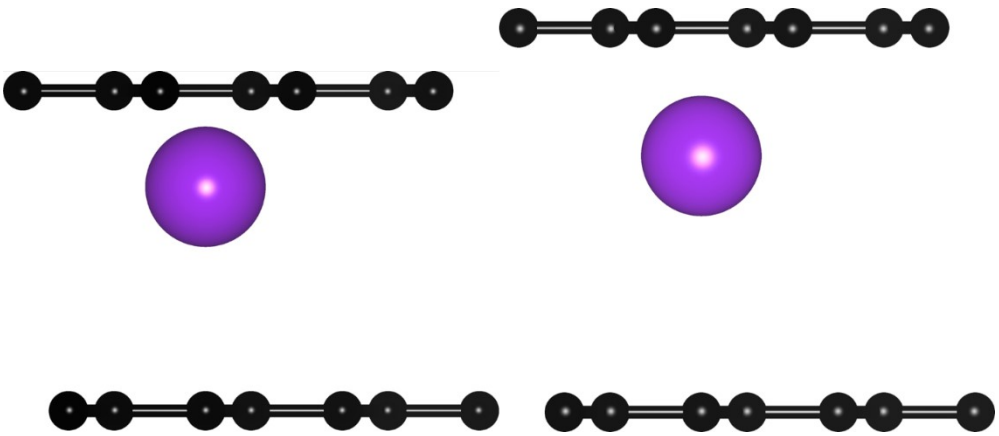

Figure S10: Configurations of K ion inserted into the planar graphitic layer with (a) 3 Å, (b) 4 Å, (c) 5 Å, and (d) 6 Å interlayer distances.

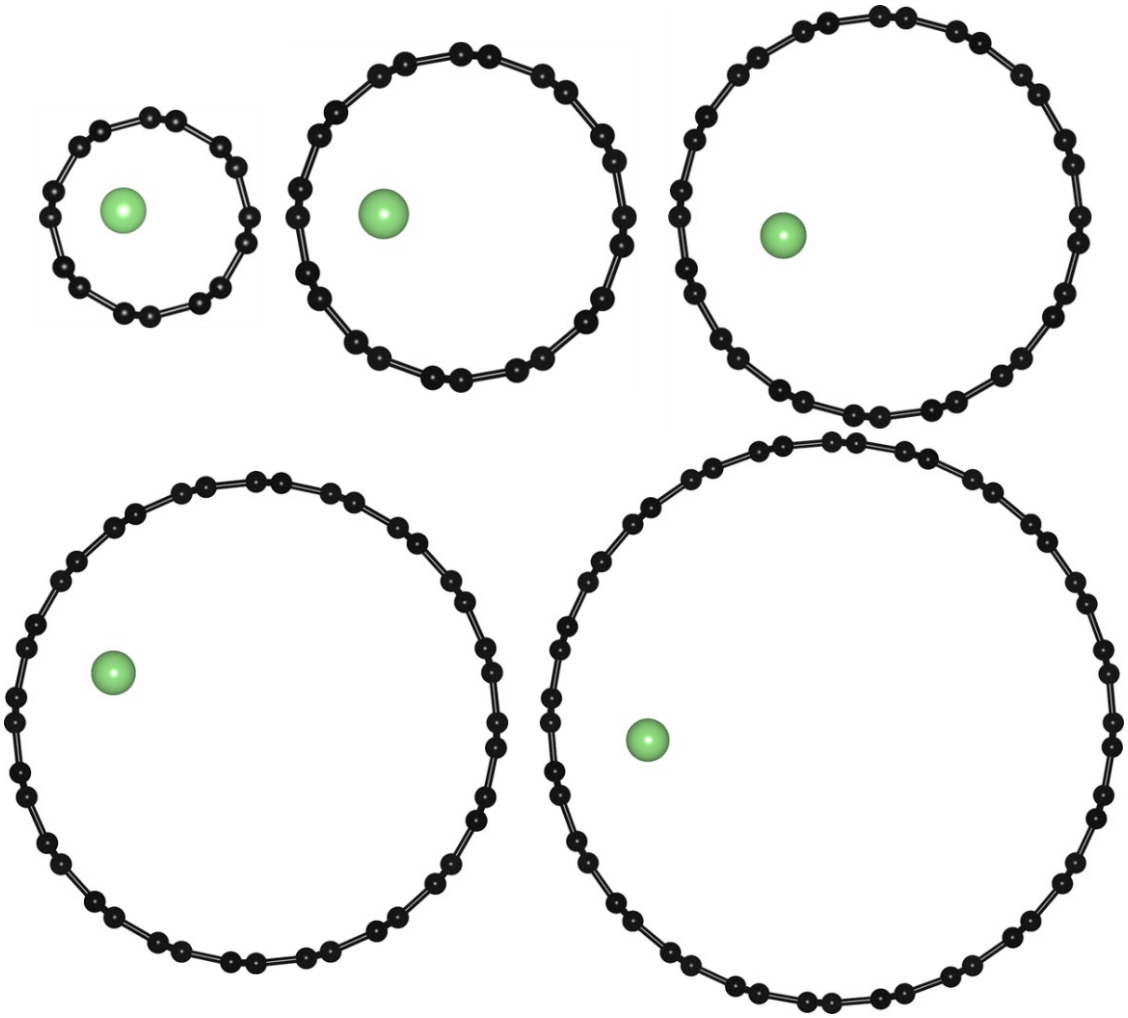

Figure S11: Configurations of Li ion intercalated into the micropores with diameters of (a) 5.424 Å, (b) 8.136 Å, (c) 10.848 Å, (d) 13.560 Å, and (e) 16.272 Å.

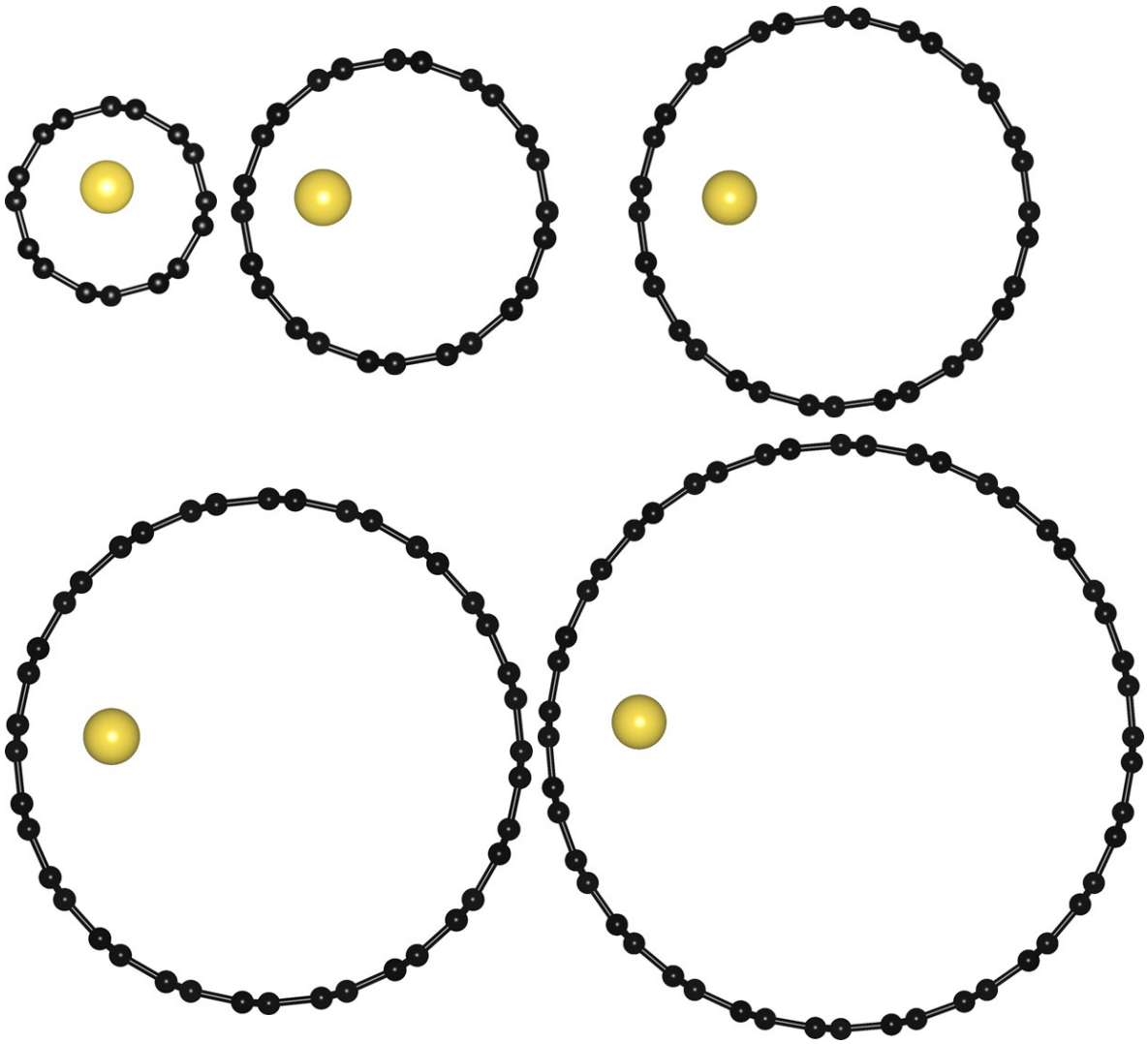

Figure S12: Configurations of Na ion intercalated into the micropores with diameters of (a) 5.424 Å, (b) 8.136 Å, (c) 10.848 Å, (d) 13.560 Å, and (e) 16.272 Å.

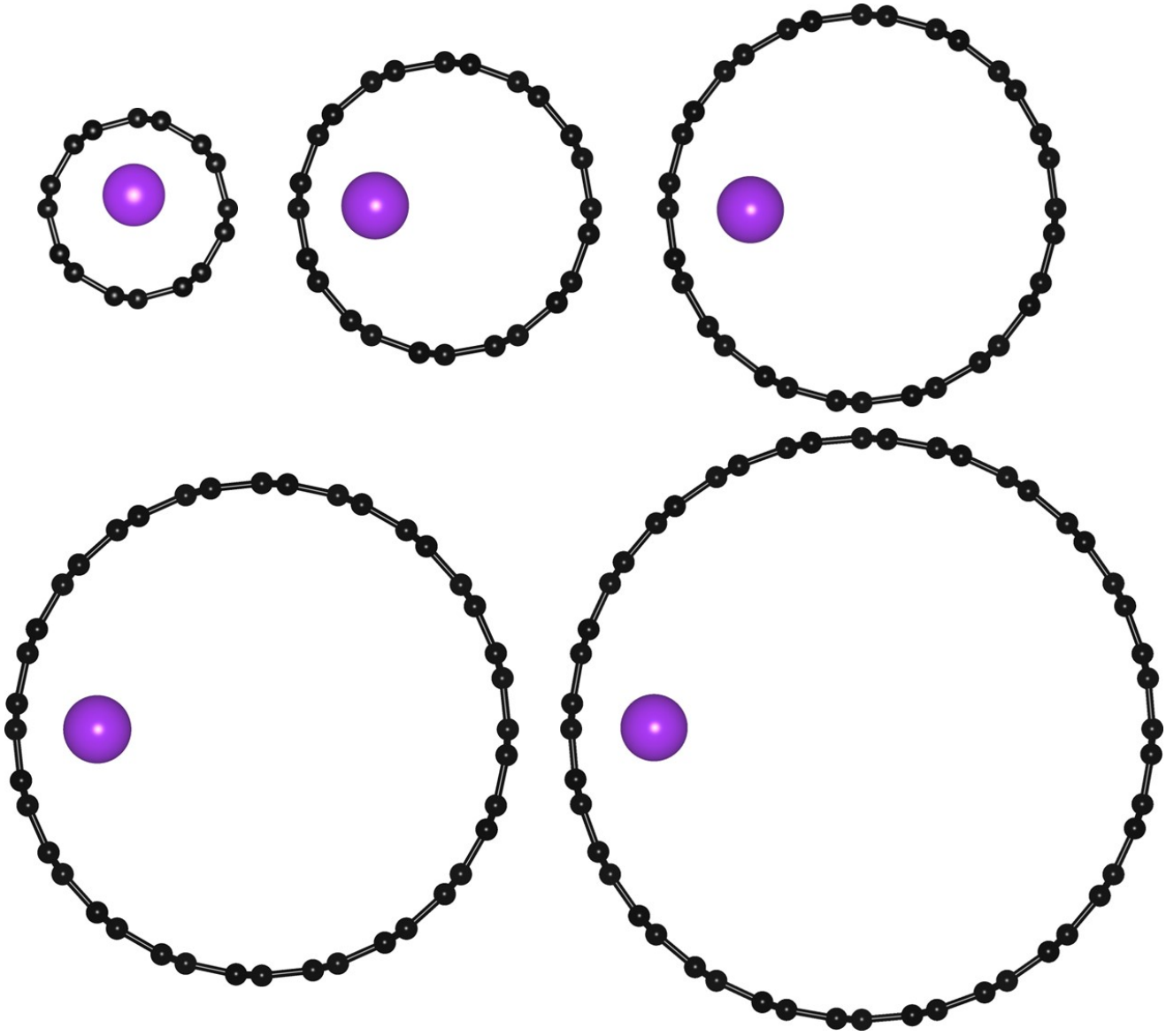

Figure S13: Configurations of K ion intercalated into the micropores with diameters of (a) 5.424 Å, (b) 8.136 Å, (c) 10.848 Å, (d) 13.560 Å, and (e) 16.272 Å.

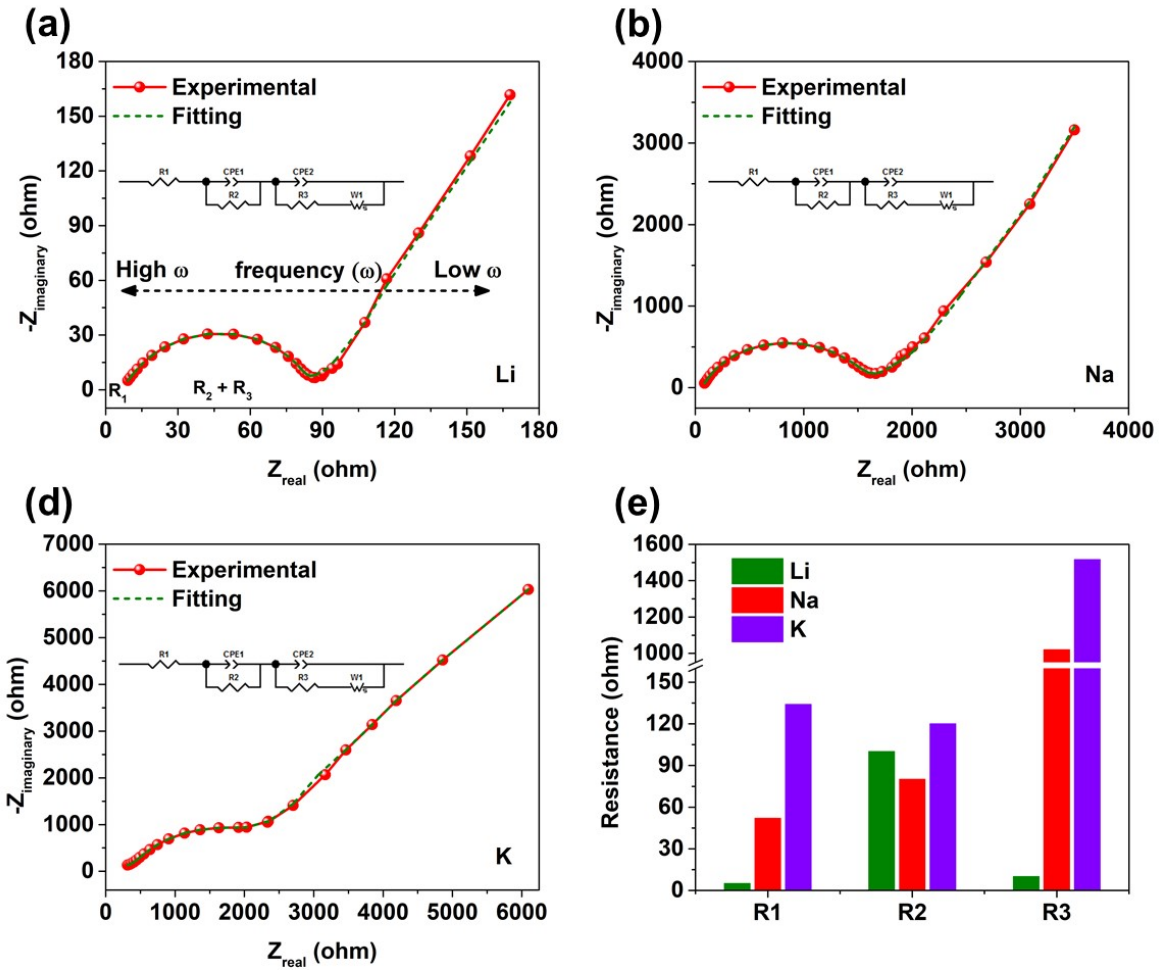

Figure S14: Nyquist plot with fitted curve of (a) MSHC/Li, (b) MSHC/Na, and (c) MSHC/K. (d) The fitted obtained value of resistances (R_1, R_2 and R_3) for Li, Na and K-cell.

Table S1: Comparative electrochemical performance of recent hard carbon anodes for sodium-ion batteries.

Precursor	**Specific capacity (mAh/g) at 0.1C**	**ICE (%)**	**Rate performance** (mAh/g at C rate)	**Long cycle**	**Plateau Capacity (%)**	**Reference**
Almond Shell	342.4 mAh/g	87.19	342 at 0.1C 250 at 1C	84.8% after 400 cycles at 1C	55%	*J. Mater. Chem. A, 2024, 12, 21176*
Sucrose	290 mAh/g	75%	280 at 0.2C 220 at 1C	52% after 500 cycles at 1C	53%	*J. Mater. Chem. A, 2023, 11, 9816*
Chitosan	386 mAh/g	77%	293 at 0.2C 181 at 2C	90% after 2000 cycles at 1 A/g	55%	*J. Mater. Chem. A, 2025, 13, 8679*
Activated Carbon	433 mAh/g	88-6%	380 at 0.2C 290 at 1C	80% after 1000 cycles at 2C	64%	*Energy Environ. Sci., 2023, **16**, 4041-4053*
PVP	350.7 mAh/g	94%	280 at 0.2C 220 at 1C	82% after 500 cycles at 1C	65%	*Energy Environ. Sci., 2024, 17, 8189*
Microcrystalline cellulose	362 mAh/g	92.4%	340 at 0.2C 200 at 2C	94% after 80 cycles at 0.1C	61%	*Adv. Funct. Mater., 2025, 35, 2423559*
Oak leave	383 mAh/g	79.6%	370 at 0.2C 310 at 2C	78% after 1150 cycles 1C	60%	*Adv. Energy Mater.2025, 15, 2403142*
Bacillus licheniformis	360 mAh/g	88.2%	348 at 0.5C 320 at 1C	79% after 200 cycles at 0.2C	65	*J. Am. Chem. Soc. 2025, 147, 10, 8088–8092*
Lotus root starch	340 mAh/g	85.6%	330 at 0.2C 290 at 1C	81% after 2000 cycles at 5C	60.3%	*Chem. Eng. J.,2025, 519, 165014.*
Macadamia nutshell	210 mAh/g	59.57%	190 at 0.5C, 140 at 1C	80% after 200 cycles at 0.5C	50.85%	*ACS Omega 2025, 10, 22, 23620–23628*
Surcose	422 mAh/g	66%	352 at 0.2C 290 at 1C	84% after 500 cycles at 1C	57%	*This work*

References:

(1) Nagmani.; Manna, S.; Puravankara, S. Hierarchically Porous Closed-Pore Hard Carbon as a Plateau-Dominated High-Performance Anode for Sodium-Ion Batteries. *Chem. Commun.* **2024**, *60* (22), 3071–3074. https://doi.org/10.1039/d4cc00025k.

(2) Joubert, D. From Ultrasoft Pseudopotentials to the Projector Augmented-Wave Method. *Phys. Rev. B - Condens. Matter Mater. Phys.* **1999**, *59* (3), 1758–1775. https://doi.org/10.1103/PhysRevB.59.1758.

(3) Vargas-Hernández, R. A. Bayesian Optimization for Calibrating and Selecting Hybrid-Density Functional Models. *Phys. Rev. B-Condens. Matter Mater. Phys* **1996**, *54* (16), 11169–11186. https://doi.org/https://doi.org/10.1103/PhysRevB.54.11169.

(4) Perdew, J. P.; Burke, K.; Ernzerhof, M. Generalized Gradient Approximation Made Simple (Vol 77, Pg 3865, 1996). *Phys. Rev. Lett.* **1997**, *78* (7), 1396–1396.

(5) Grimme, S.; Antony, J.; Ehrlich, S.; Krieg, H. A Consistent and Accurate Ab Initio Parametrization of Density Functional Dispersion Correction (DFT-D) for the 94 Elements H-Pu. *J. Chem. Phys.* **2010**, *132* (15). https://doi.org/10.1063/1.3382344.

(6) Li, Z. H. A Program for SAXS Data Processing and Analysis. *Chinese Phys. C* **2013**, *37* (10). https://doi.org/10.1088/1674-1137/37/10/108002.

(7) Yuan, M.; Cao, B.; Liu, H.; Meng, C.; Wu, J.; Zhang, S.; Li, A.; Chen, X.; Song, H. Sodium Storage Mechanism of Nongraphitic Carbons: A General Model and the Function of Accessible Closed Pores. *Chem. Mater.* **2022**, *34* (7), 3489–3500. https://doi.org/10.1021/acs.chemmater.2c00405.

(8) Li, A.; Tong, Y.; Cao, B.; Song, H.; Li, Z.; Chen, X.; Zhou, J.; Chen, G.; Luo, H. MOF-Derived Multifractal Porous Carbon with Ultrahigh Lithium-Ion Storage Performance. *Sci. Rep.* **2017**, *7*, 1–8. https://doi.org/10.1038/srep40574.